



# Construction of ZnO/TiO<sub>2</sub> photonic crystal heterostructures for enhanced photocatalytic properties

Xiuzhen Zheng, Danzhen Li\*, Xiaofang Li, Jing Chen, Changsheng Cao, Jialin Fang, Jubao Wang, Yunhui He, Yi Zheng

Research Institute of Photocatalysis, State Key Laboratory of Photocatalysis on Energy and Environment, Fuzhou University, Fuzhou 350002, PR China

## ARTICLE INFO

### Article history:

Received 18 November 2014

Received in revised form

30 December 2014

Accepted 4 January 2015

Available online 6 January 2015

### Keywords:

ZnO nanoparticles

TiO<sub>2</sub> photonic crystal

Photocatalysis

Heterostructures

Active species

## ABSTRACT

A highly ordered ZnO/TiO<sub>2</sub> photonic crystal (ZnO/TiO<sub>2</sub>-PC) was obtained by a simply pyrolysis strategy. Combined with a series of characterizations, including scanning electron microscopy (SEM), transmission electron microscopy (TEM), X-ray photoelectron spectroscopy (XPS), X-ray diffraction (XRD) and transmittance spectra, it was found that the in situ formed ZnO phases were uniformly grafted to TiO<sub>2</sub>-PC framework forming hybrid nanostructure. Additionally, the formation of heterojunction between ZnO and TiO<sub>2</sub>-PC enhanced the separation efficiency of photogenerated electron–hole pairs, which significantly improved the photocatalytic performances. Based on the results of photoelectrochemical measurement and the detection of active species in photocatalytic degradation process, the photocatalytic degradation mechanism of ZnO/TiO<sub>2</sub>-PC nanocomposite was proposed. It is hoped that our work could provide a good insight into the preparation of photonic crystal heterostructures for the environmental purification.

© 2015 Elsevier B.V. All rights reserved.

## 1. Introduction

Heterogeneous photocatalysis by use of semiconductor materials has been applied as an efficient method in the field of environmental purification. TiO<sub>2</sub> is generally believed to be the most reliable material for the degradation of organic compounds due to its non-toxicity, low cost, physical and chemical stability, and high reactivity [1,2]. To date, various structures of TiO<sub>2</sub> photocatalysts, such as wires, rods, tubes, flakes, spheres, and porous structures, have been fabricated for their special physicochemical properties [3–9]. Among these different morphologies, one of the important porous structures is photonic crystal, and TiO<sub>2</sub> photonic crystal (TiO<sub>2</sub>-PC) has recently attracted significant interest due to its impressive properties, such as photonic band gap (PBG) scattering effect, and slow photon effect. It has been used in the field of water splitting [10,11], solar cells [12,13], and pollutants decomposition [14,15]. For photonic crystals photocatalyst, one of the most intriguing properties for periodic photonic structures is the high surface/volume fractions and interconnected pores, which indicates highly functional features of TiO<sub>2</sub> with regular and controllable nanoscale geometry. Therefore, to study on the

nanocomposite of photonic crystal is significant for the TiO<sub>2</sub>-PC-based photocatalysts to broaden the application of photocatalysis.

As is known, the practical application of pure TiO<sub>2</sub>-PC is limited by the low quantum efficiency [7,16]. To exploit effective photocatalysts with lower recombination rate of charge carriers, a variety of strategies have been employed to improve the efficiency of TiO<sub>2</sub>-PC photocatalytic degradation, such as prolonging electron and hole lifetimes through doping and incorporating metals [17,18], or increasing surface area by making it mesoporous in the wall [19]. In addition to these modifications, coupling TiO<sub>2</sub>-PC with other semiconductors has been proven to be a feasible approach in separating photogenerated electron–hole pairs. In recent years, tremendous efforts have been devoted to developing photocatalysts with high activity by constructing the heterojunction between TiO<sub>2</sub>-PC and other semiconductors. It is still a giant challenge to prepare TiO<sub>2</sub>-PC heterostructure materials because of the structural complexity and control difficulty in the crystal growth of two different materials.

Among various semiconductor oxides, TiO<sub>2</sub> and ZnO (with wide band gaps about 3.2 eV and 3.37 eV, respectively) are two kinds of great technologically important materials due to their excellent electronic, chemical and optical properties [20,21]. ZnO is also an excellent *n*-type semiconductor exhibiting comparable efficiency for various photocatalytic reactions [22,23], when compared with TiO<sub>2</sub>. Moreover, potentials of the conduction band and valence band of ZnO are a bit more negative than TiO<sub>2</sub>. The

\* Corresponding author. Tel.: +86 591 83779256; fax: +86 591 83779256.  
E-mail address: [dzli@fzu.edu.cn](mailto:dzli@fzu.edu.cn) (D. Li).

heterojunction between  $\text{TiO}_2$  and  $\text{ZnO}$  can result in the injection of conduction band electrons from  $\text{ZnO}$  to  $\text{TiO}_2$ , which is helpful for electron–hole separation [21,24]. Therefore, incorporating two of these materials into an integrated structure is of great significance because the resulting products may possess the improved physical and chemical properties. Inspired by this, combined with structural advantages of  $\text{TiO}_2$ -PC, the highly ordered  $\text{ZnO}/\text{TiO}_2$ -PC hybrid nanostructure with promising photocatalytic efficiency can be expected.

Herein, we reported a pyrolysis route to construct 3-D highly ordered  $\text{ZnO}/\text{TiO}_2$ -PC heterostructure, by which in situ formed  $\text{ZnO}$  nanoparticles (NPs) were evenly grafted on the surface of  $\text{TiO}_2$ -PC framework (more on the inner surface, less on the outer surface). The morphologies, crystal phases, optical properties and photocatalytic performances of the  $\text{ZnO}/\text{TiO}_2$ -PC heterostructures were explored to clarify the structure–property correlation. The active species in the photocatalytic degradation process were investigated, and underlying mechanism responsible for well-defined morphology of the  $\text{ZnO}/\text{TiO}_2$ -PC heterostructure was tentatively probed. The results showed that the enhanced separation efficiency of electron–hole pairs and excellent photostability of the  $\text{ZnO}/\text{TiO}_2$ -PC heterostructure have been attained, owing to the formation of heterojunction structure which intimately combines  $\text{ZnO}$  with  $\text{TiO}_2$ -PC. It is hoped that our work may provide new insights into the preparation of 3D photonic crystal hybrid nanostructures for the environmental purification.

## 2. Experimental

### 2.1. Materials

All solvents and chemicals were of analytical grade. Titanium isopropoxide, diethanolamine, and zinc nitrate [ $\text{Zn}(\text{NO}_3)_2$ ] (Aldrich) were used as the precursors to prepare  $\text{ZnO}/\text{TiO}_2$ -PC heterostructures. *Tert*-butyl alcohol (TBA), ammonium oxalate (AO), and benzoquinone (BQ) were from Sinopharm Chemical Reagent Co., Ltd. Water used in all experiments was deionized water.

### 2.2. Preparation of the $\text{ZnO}/\text{TiO}_2$ -PC heterostructures.

$\text{ZnO}/\text{TiO}_2$ -PC heterostructures were prepared by depositing  $\text{ZnO}$  on  $\text{TiO}_2$ -PC via a pyrolysis approach. The polystyrene (PS) template with the three-dimensional ordered structures was obtained by vertical deposition method. The PS templates with the average sizes of 300 nm was prepared and denoted as PS300 (Supporting information, Figure S1). After impregnating and calcination treatment, the  $\text{TiO}_2$ -PC was obtained and labeled as T300 (corresponding for the  $\text{TiO}_2$ -PC fabricated using PS300), according to our previous work [14]. A designated amount (1.075 g, 2.15 g, 3.225 g, and 4.3 g) of  $\text{Zn}(\text{NO}_3)_2$  was added to ethanol aqueous solution (i.e., 7.5 g of ethanol plus 14 g of  $\text{H}_2\text{O}$ ). Then, T300 was immersed in the above solutions for 2 h, and dried by  $\text{N}_2$  flow. It should be emphasized that the loading percentage defined as weight ratio of  $\text{Zn}(\text{NO}_3)_2$  to ethanol aqueous solution were 5%, 10%, 15%, and 20%, respectively. Subsequently, the pretreated samples were annealed at 400 °C for 3 h in air with the heating rate of 1 °C/min to transform absorbed precursor to  $\text{ZnO}$  phase, and a series of  $\text{ZnO}/\text{T300}$  (ZT300) nanocomposite were labeled as ZT300@5%, ZT300@10%, ZT300@15%, and ZT300@20%, respectively. The corresponding Zn/Ti ratio was about 0.31/1, 0.62/1, 1.03/1, and 1.23/1 by calculating the mass of  $\text{ZnO}$  and  $\text{TiO}_2$ , respectively. Meanwhile, P25 particulate film was fabricated for comparison, and the film was deposited on microslide using a slurry of 20 wt % P25  $\text{TiO}_2$  in ethanol.

### 2.3. Characterization of samples

The general morphologies of the products were examined by field emission scanning electron microscopy (FESEM) on a SU 8010 instrument operated at 5 kV. Transmission electron microscopy (TEM), high-resolution TEM (HRTEM) images, and energy-dispersive X-ray spectrometer (EDX) were obtained by using a FEI Tecnai G2 F20 instrument operated at an accelerating voltage of 200 kV. The X-ray diffraction (XRD) patterns were determined by a Bruker D8 Advance X-ray diffractometer with  $\text{Cu K}\alpha$  radiation. The accelerating voltage and applied current were 40 kV and 40 mA, respectively. X-ray photoelectron spectroscopy (XPS) analysis was collected on an ESCALAB 250 photoelectron spectrometer (Thermo Fisher Scientific) with monochromatic  $\text{Al K}\alpha$  radiation ( $E = 1486.2$  eV). All of the binding energies were calibrated by the C 1s peak at 284.6 eV. Brunauer–Emmett–Teller surface area of the samples was measured via  $\text{N}_2$  adsorption at 77 K by using ASAP2020M analyzer from Micromeritics Instrument Corporation. The photoelectrochemical data was collected by a CHI-660D electrochemical workstation (Chenhua Instruments, Co., Shanghai). The photoelectrochemical experiment was carried out in a conventional three-electrode cell with a quartz window. The sample was deposited on a sheet of fluorine-tin-oxide (FTO) glass to serve as the working electrode with 2 cm  $\times$  3 cm area. A platinum wire and an Ag/AgCl electrode were used as the counter and reference electrodes, respectively. The electrolyte was 0.1 M  $\text{Na}_2\text{SO}_4$  solution. Electron spin resonance (ESR) spectra were obtained using a Bruker model A300 spectrometer with a 500 W Xe-arc lamp equipped with an IR-cut-off filter (320 nm  $< \lambda < 800$  nm) as light source. The photoluminescence (PL) spectra were collected on an Edinburgh FL/FS900 fluorescence spectrometer. The generation of hydroxyl radical ( $\cdot\text{OH}$ ) was investigated by the PL technique with terephthalic acid (TA) as a probe molecule. The optimal concentration of TA solution was  $5 \times 10^{-3}$  M in a diluted NaOH aqueous solution ( $1 \times 10^{-2}$  M) [25,26]. Nitroblue tetrazolium (NBT,  $2 \times 10^{-5}$  M, exhibiting an absorption maximum at 259 nm) was used to determine the amount of superoxide radical ( $\text{O}_2^{\cdot-}$ ) generated from ZT300@15% and T300 system [27,28]. The method was similar to the latter photocatalytic activity test with NBT replacing the MO.  $\text{H}_2\text{O}_2$  was determined by a photometric method in which DPD is oxidized by a POD catalyzed reaction, with the absorption peaks at 510 and 551 nm [29]. After 30 min of simulated solar light irradiation, the  $\text{TiO}_2$  film was removed from the  $\text{TiO}_2/\text{H}_2\text{O}$  system, and the water was analyzed to detect the formation of  $\text{H}_2\text{O}_2$ .

### 2.4. Photocatalytic activity

Photocatalytic activity was evaluated by using methyl orange (MO) as a model organic dye pollutant compound. In the typical test, samples with the same area of 3 cm  $\times$  2 cm were soaked into 10 mL of MO aqueous solution (5 mg/L) in a quartz cuvette. Before irradiation, the mixtures were kept in the dark for 30 min to reach equilibrium of adsorption–desorption at room temperature. A 500-W Xe-arc lamp (Institute of Electric Light Source, Beijing) equipped with an IR-cut-off filter (320 nm  $< \lambda < 800$  nm) was applied as the simulated solar light source. A small aliquot was withdrawn at each given time interval and analyzed using a Varian Cary 50 Scan UV–vis spectrophotometer. After the concentration of the solution was monitored by the absorption peak at 464 nm, the analyzed aliquot was quickly poured back into the reactor. The photocatalytic degradation ratio was recognized as  $(1 - C_t/C_0) \times 100\%$ , where  $C_0$  was the adsorption equilibrium concentration of solution, and  $C_t$  was the concentration of solution at time  $t$ .

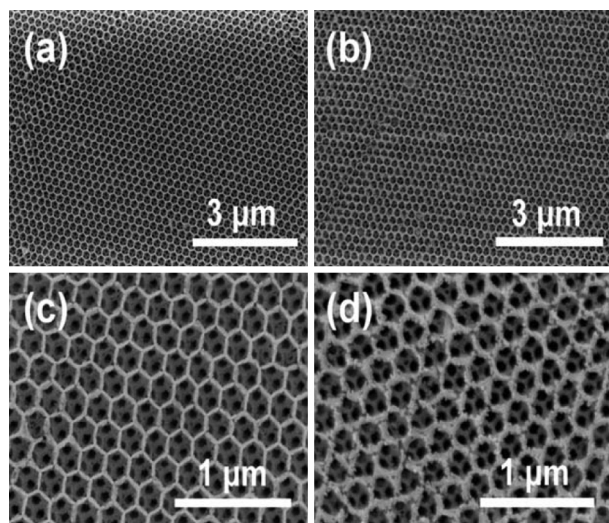


Fig. 1. FESEM images of (a and c) T300 and the as-prepared (b and d) ZT300@15% nanocomposite.

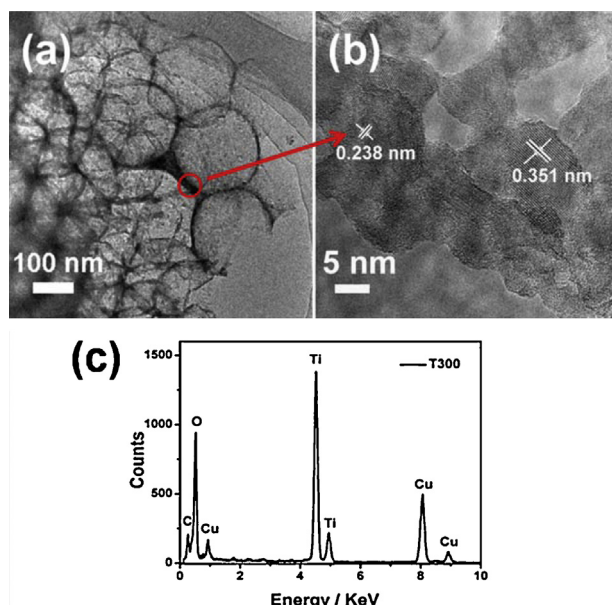


Fig. 2. TEM images and EDX spectrum of the synthesized T300: (a) low-magnification, (b) high-magnification, and (c) EDX spectrum.

### 3. Results and discussion

#### 3.1. Preparation of the well-defined ZnO/TiO<sub>2</sub>-PC heterostructure

The morphologies of T300 and ZT300@15% nanocomposite were examined by FESEM (Fig. 1). As shown in Fig. 1a and c, it could be observed that T300 exhibited well-ordered periodic structure with few defects, and the pore size was uniform with an average pore diameter of 215 nm. When ZnO was deposited on the surface of T300, the hybrid nanostructure of ZT300@15% sample (Fig. 1b and d) was obviously different from that of T300. Although it well duplicated the highly ordered structure of T300 to form a periodic structure, its skeleton was thickening. The mean diameter was narrowed to 205 nm. It could be tentatively deduced that in situ produced ZnO phases were intimately embedded on the surface of T300.

The TEM images and EDX patterns of T300 and ZT300@15% hybrid nanostructure were shown in Fig. 2 and Fig. 3. The

crystal structure of T300 was examined, and its ring shape can be seen clearly from the TEM image shown in Fig. 2a. The lattice fringes with the spacing of 0.352 and 0.238 nm could be observed from the HRTEM image (Fig. 2b), corresponding to the interplanar distances of (101) and (004) facets of anatase TiO<sub>2</sub>. Only Ti and O were detected in the EDX pattern of T300 (Fig. 2c). The detection of C and Cu was originated from carbon-coated copper grid used for the TEM measurement. Therefore, the final materials of T300 possessed high purity, which was important to guarantee a good index of refraction inside the inverse opal structure.

Meanwhile, the ring shape of ZT300@15% could be seen clearly from the TEM image (Fig. 3a), which agreed with SEM results. As shown in Fig. 3b, high-resolution TEM image was taken at the skeleton of ZT300@15% nanocomposite, and many different lattice fringes could be found, which allowed for the identification of crystallographic spacing of TiO<sub>2</sub> and ZnO. The lattice fringes of 0.352 and 0.282 nm concurred well with interplanar spacing of (101) and (100) crystallographic planes of TiO<sub>2</sub> and ZnO. The nanostructured heterojunction was formed in ZnO/TiO<sub>2</sub> nanocomposite, and T300 was tightly wrapped by the ZnO NPs (~15 nm, Fig. 3c). Furthermore, composition elements of the ZT300@15% nanocomposite were demonstrated in the EDX pattern (Fig. 3b and d), consisting of Ti, Zn, and O from the nanocomposite. Thus, TEM and EDX results further revealed that the pyrolysis approach developed in our work was beneficial for creating ZT300@15% heterostructure, in which the second phase of ZnO NPs were grafted on the surface of T300.

Crystal structure of the T300, ZT300@15%, and ZnO samples was determined by XRD, as shown in Fig. 4. The peaks of T300 at  $2\theta$  values of 25.3°, 37.8°, 48.0°, 53.9°, and 62.7° were undisputedly indexed to (101), (004), (200), (105), and (204) crystal planes of anatase TiO<sub>2</sub> (JCPDS no. 21-1272), respectively. The pattern of ZnO could be readily indexed to a pure monoclinic phase with lattice constants to be comparable with the values given in hexagonal wurtzite-type ZnO (JCPDS no. 36-1451), and no traces of other phases were examined. Combined with SEM and TEM results, it should be emphasized that crystal phase of the ZT300@15% nanocomposite were displayed in Fig. 4, in which anatase TiO<sub>2</sub> and ZnO formed the dominant phases. The sharp and intense diffraction peaks suggested a high crystallinity of the samples.

To further uncover the composition of the samples, XPS was employed to probe surface property of the ZT300@15% nanocomposite. Gaussian deconvolution of the high-resolution spectra was

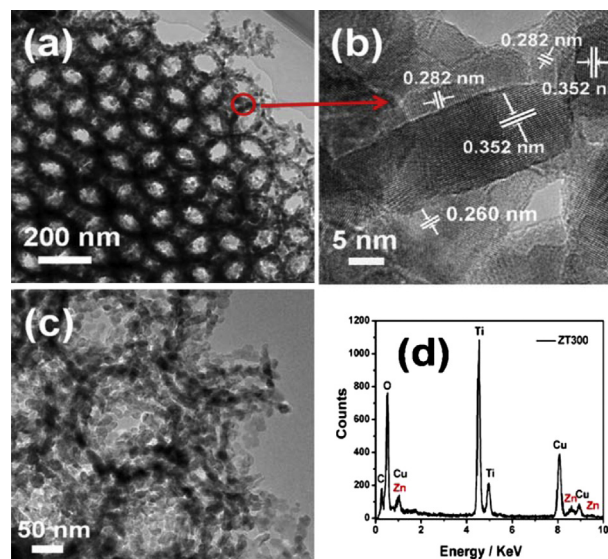


Fig. 3. TEM images and EDX spectrum of the synthesized ZT300@15%: (a and c) low-magnification, (b) high-magnification, and (d) EDX spectrum.



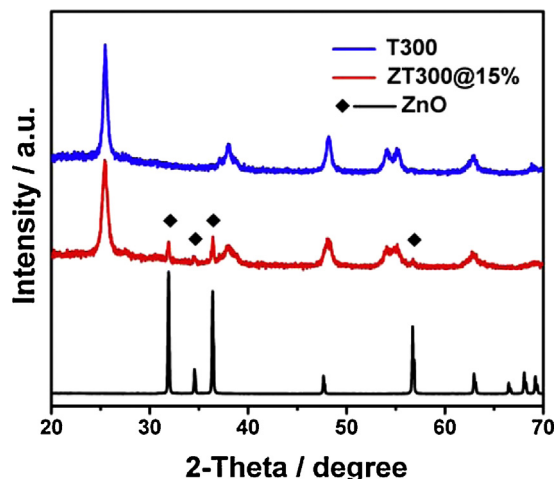


Fig. 4. XRD patterns of T300, ZT300@15% nanocomposite, and ZnO.

applied to differentiate varied chemical bond species, and particularly, chemical states of elements for ZT300@15% and T300. As shown in Figure S2, ZT300@15% nanocomposite was mainly composed of four elements: C 1s, O 1s, Ti 2p, and Zn 2p. For C 1s spectrum (Fig. 5 a), the major peak with binding energy (BE) at 284.60 eV was attributed to surface C–C or C–H bonds, and the second peak 286.03 eV was attributed to carbon atoms presented in surface C–OH or C–O–C groups. The third peak at 288.52 eV was assigned to surface –COO–group. As for O 1s spectrum (Fig. 5b), the highest peak at 529.55 eV was attributed to lattice oxygen in

the  $\text{TiO}_2$  and ZnO (i.e., Ti–O and Zn–O). The peak at 530.32 eV was assigned to the oxygen in surface hydroxyl groups for  $\text{TiO}_2$  and ZnO (i.e., Ti–OH and Zn–OH), and the peak at 531.47 eV was assigned to the oxygen in C–OH/C–O–C corresponding to the C 1s specie at 286.03 eV. As shown in Fig. 5c, featured peaks with BE of 458.25 eV (Ti 2p<sub>3/2</sub>) and 464.10 eV (Ti 2p<sub>1/2</sub>) in core-level spectrum of Ti agreed with anatase  $\text{TiO}_2$  ( $\text{Ti}^{4+}$ ). High-resolution spectrum of Zn 2p (Fig. 5d) displayed characteristic peaks of 1021.40 eV (Zn 2p<sub>3/2</sub>) and 1044.34 eV (Zn 2p<sub>1/2</sub>) corresponding to chemical element state of  $\text{Zn}^{2+}$  (ZnO).

Table S1 displayed detailed chemical bond species versus BE for the T300 and ZT300@15% nanocomposite. It was noted that lattice oxygen of T300 (i.e., Ti–O) exhibited pronounced BE shift of 0.30 eV (529.25 vs 529.55 eV) [30]. Moreover, Ti 2p<sub>3/2</sub> and Ti 2p<sub>1/2</sub> species of T300 also demonstrated BE shifts of 0.25 eV (458.00 vs 458.25 eV) and 0.22 eV (463.88 vs 464.10 eV) [30], which corroborated perturbation of Ti–O bonds in T300 with the functionalization of ZnO. Based on the above analysis, the heterostructures were formed in ZT300 nanocomposite due to that the well-defined morphology and intimate interfacial contact between T300 and ZnO.

Transmittance spectra were utilized to determine the optical properties of these samples. It is well-known that PBG is one of the most important features for photonic crystals. The PBGs of the T300 and ZT300@15% nanocomposite were measured in the air (Fig. 6a), and PBGs were centered at around 395 and 390 nm, respectively. The PBG of ZT300@15% was blue shift due to that ZnO was grown on the surface of T300. In the water, the photonic band gap of T300 and ZT300@15% were centered at around 475 and 460 nm (Fig. 6b). Additionally, the absorption peak of MO was about 464 nm, overlapped with the photonic band gap of ZT300@15% in

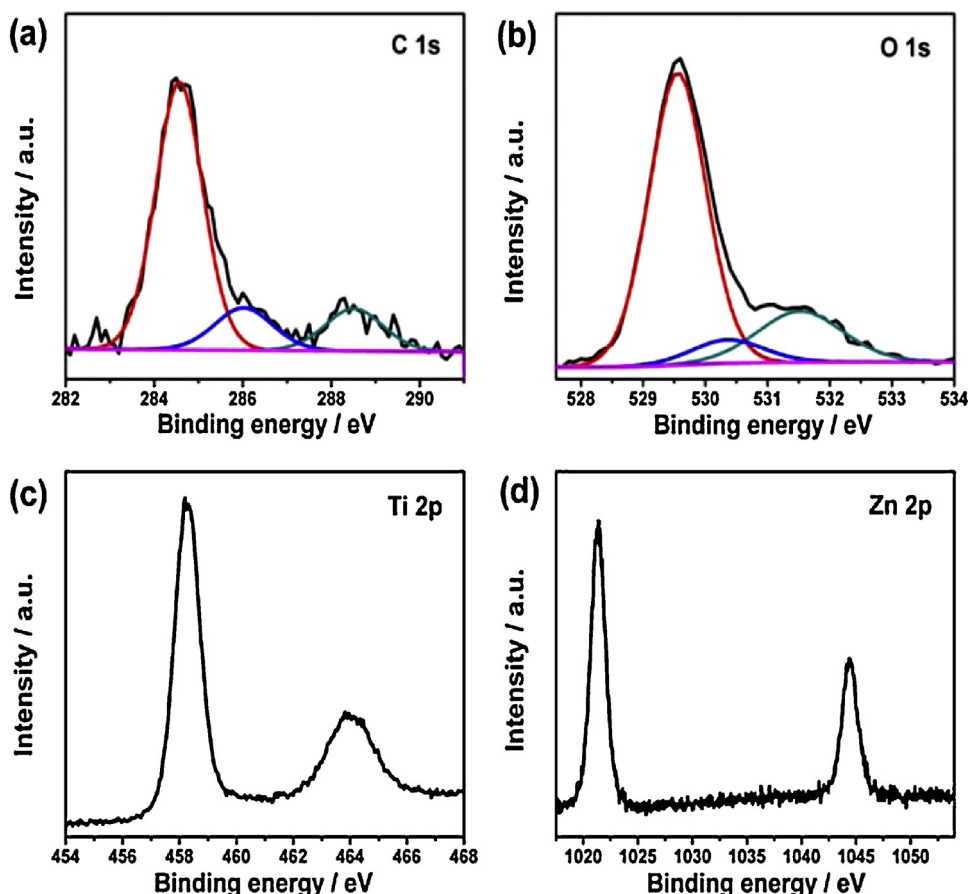


Fig. 5. High-resolution XPS spectra of (a) C 1s, (b) O 1s, (c) Ti 2p, and (d) Zn 2p for the ZT300@15% nanocomposite.

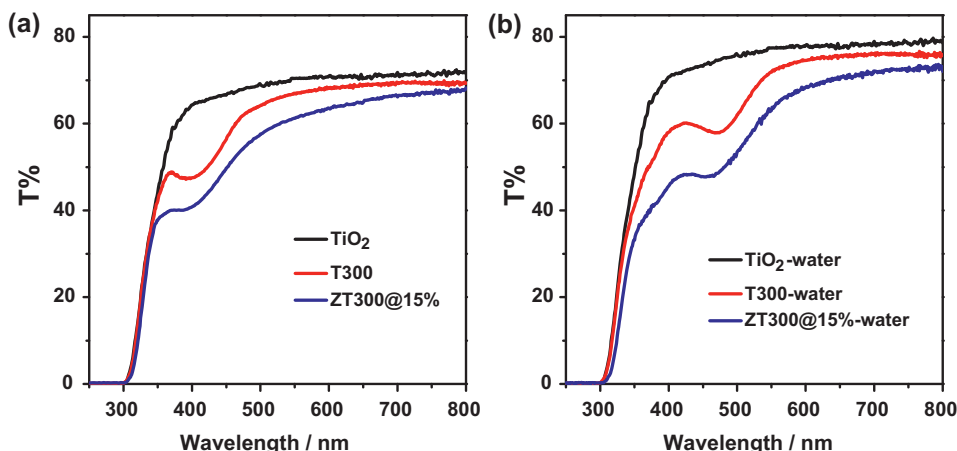


Fig. 6. Transmittance spectra of T300 and ZT300@15% nanocomposite in the air (a) and water (b).

the water. When MO was adsorbed on the surface of the ZT300@15% and matched with the photonic band gap of ZT300@15%, the slow photon effect would enhance the interaction between MO and photocatalyst, which was beneficial for the photocatalytic degradation [14]. Therefore, MO was chosen as the target probe molecule to evaluate the photocatalytic capability of the ZT300 under simulated solar light irradiation.

To recapitulate, combinatorial results of SEM, TEM, XPS, XRD, and transmittance spectra indicated successful preparation of well-defined ZT300 heterostructures via a pyrolysis approach. The in situ formed ZnO NPs were uniformly grafted on T300 surface based on intimate interfacial contact between ZnO and surface of TiO<sub>2</sub>. In addition, the formation of ZT300 nanocomposite might be attributed to three reasons. First, super hydrophilicity of the TiO<sub>2</sub> surface was highly advantageous for absorbing polar aqueous precursor to make Zn(NO<sub>3</sub>)<sub>2</sub> completely impregnate into interior and external surfaces of the T300, thus beneficial for the uniform distribution of ZnO NPs. Second, negatively charged TiO<sub>2</sub> layer was beneficial for spontaneous absorption of Zn<sup>2+</sup> on the T300 surface via substantial electrostatic interaction force. Third, intimate interfacial interaction between ZnO and TiO<sub>2</sub> via chemical bonding was also speculated to be responsible for the well-defined morphology of the heterostructure, which could be revealed by XPS result.

### 3.2. Photocatalytic performance of the ZT300 nanocomposite

MO was used as the target probe molecule for photocatalytic degradation reactions to evaluate the photocatalytic capability of the ZT300@15% and T300 under simulated solar light irradiation. The photocatalytic activity of ZT300@15% nanocomposite for liquid-phase degradation was measured at room temperature, and the P25 film was used as the reference catalysts. Blank experiment (i.e., only light irradiation without catalysts) showed negligible photocatalytic activity, corroborating the degradation reaction was truly driven by a photocatalytic process. As shown in Figure S3, the photocatalytic activity of the T300 for liquid-phase degradation was measured, and the TiO<sub>2</sub> porous (TiO<sub>2</sub>-P) film and TiO<sub>2</sub> nanoparticle (TiO<sub>2</sub>-NP) film were used as the reference catalysts. For T300 film, its unique inverse-opal structure would enhance the light absorption within the catalyst, while the TiO<sub>2</sub>-P film harvested the light just on its surface. Thus, the photocatalytic degradation efficiency of MO followed the order: T300 > TiO<sub>2</sub>-P > TiO<sub>2</sub>-NP > blank, illuminating that the presence of inverse-opal structure played an essential role in affecting photocatalytic activity.

After 120 min of simulated solar light irradiation (Fig. 7), the photocatalytic conversion ratios of MO for TiO<sub>2</sub>-NP, ZnO-NP, ZnO/TiO<sub>2</sub>-NP, T300, P25, and ZT300@15% were 20%, 30%, 51%, 78%, 90%, and 95%, respectively. ZT300@15% nanocomposite (Figure S4) still exhibited remarkably superior photocatalytic activity to its counterparts of P25 particulate film, ZnO film and T300. The corresponding mineralization ratios of the samples ZnO/TiO<sub>2</sub>-NP, P25 and ZT300@15% for MO degradation were 65.8%, 85.3% and 77.4%, respectively. Although the mineralization ratio of ZT300@15% was slightly lower than P25, ZT300@15% still have higher mineralization ratio than other samples (shown in Table S2 in detail). The enhancement of the ZT300@15% nanocomposite might arise from 2-fold cumulative contributions: (1) inverse-opal structure of ZT300 enhanced light harvesting as a result of the increased path length of light within the catalysts when compared with the ZnO bulk material (the surface areas of ZT300@15% and ZnO-NP were 34.7 and 4.1 m<sup>2</sup>/g, respectively); (2) the heterojunction effect between ZnO and TiO<sub>2</sub> increased the separation efficiency of the photogenerated electron-hole pairs. Moreover, photocatalytic activities of the ZT300 nanocomposite with different loading percentage of precursor were also tailored. As displayed in Figure S5, ZT300@15% nanocomposite still maintained the superior activity

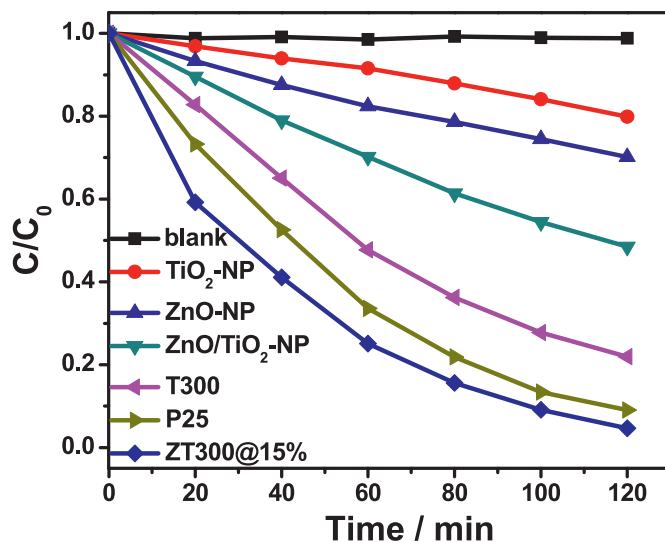
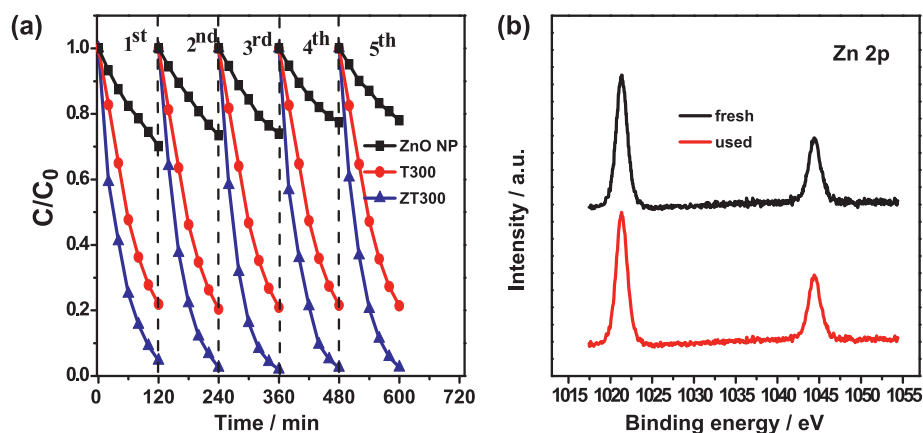


Fig. 7. Photocatalytic activities of blank (without catalyst), TiO<sub>2</sub>-NP film, ZnO-NP film, ZnO/TiO<sub>2</sub>-NP film, T300 film, P25 film, and ZT300@15% film for MO degradation under simulated solar light irradiation (320 nm < λ < 800 nm).



**Fig. 8.** (a) Cycling photodegradation of MO aqueous solution over ZnO-NP film, T300 film, and ZT300@15% film. (b) High-resolution XPS spectra of Zn 2p before and after recycled photocatalytic reactions over the ZT300@15% nanocomposite.

among the varied weight loading percentage of  $\text{Zn}(\text{NO}_3)_2$ , indicating that it was the optimal value in our system for deposition of ZnO phase.

Moreover, the stability of the ZT300@15% nanocomposite was evaluated repeatedly five times in terms of performing the MO degradation under simulated solar light irradiation (Fig. 8a). ZT300@15% and T300 exhibited better photocatalytic stability than that of the ZnO-NP film in the cycling runs of MO degradation reaction, illuminating that photonic crystal structure played an essential role in affecting photoreactivity. Especially, the photocatalytic efficiency of ZT300@15% performed some increase after the reaction being repeated five times. On the basis of XRD and XPS analysis of used sample and fresh sample (Figure S6 and Fig. 8b), the chemical state of photocatalyst did not change after the photocatalytic reaction. Therefore, it was believed that ZT300 nanocomposite possessed excellent photocatalytic activity and stability which was crucial to assess a photocatalyst and its application.

### 3.3. Discussion of photocatalytic mechanism

The transient photocurrent response has been demonstrated to be a useful technique for investigating the separation efficiency of photogenerated electron-hole pairs [31,32]. The anodic photocurrent produced by the simulated solar light irradiation was observed with good reproducibility. As shown in Fig. 9, the photocurrent response of the ZT300@15% nanocomposite was nearly 2-fold higher than that of T300, suggesting that ZT300@15% possessed more efficient separation and longer lifetime of photoexcited electron-hole pairs than that of T300. On the other hand, electrochemical impedance spectroscopy (EIS) nyquist plots of T300 and ZT300@15% (Figure S7) reflected the impedance arc radius of the ZT300@15% nanocomposite was smaller than that of T300. The results of EIS plot demonstrated that the efficiency of the separation of photogenerated electron-hole pairs increased in the order of ZT300@15% > T300. In this regard, the result was in good agreement with the photocurrent measurements.

The presence of inverse-opal structure and heterostructures in the ZT300 nanocomposite could effectively facilitate the separation of electron-hole pairs, which might cause more radical species with strong oxidation capability, such as  $\cdot\text{OH}$  and  $\text{O}_2^{\cdot-}$  species, for the MO degradation. In order to further confirm that, ESR spin-trapping technique with 5,5-Dimethyl-1-pyrroline-N-oxide (DMPO) was carried out to detect the active species under simulated solar light irradiation [33]. The intensity of ZT300@15% for

DMPO- $\cdot\text{OH}$  and DMPO- $\text{O}_2^{\cdot-}$  was much higher than that of T300 (Fig. 10 a and b).

In addition, PL-TA technique was also used to monitor the amount of  $\cdot\text{OH}$  in the ZT300@15% and T300 systems, which have been widely used in the detection of  $\cdot\text{OH}$  [29]. Fig. 10c showed the PL intensity of ZT300@15% and T300 in aqueous TA solution. It was found that the intensity of ZT300@15% was higher than that of T300, indicating that ZT300@15% produced more amount of  $\cdot\text{OH}$ . To further ascertain the change of  $\text{O}_2^{\cdot-}$ , a colorless molecular probe, nitroblue tetrazolium (NBT) was chosen to quantify the  $\text{O}_2^{\cdot-}$  concentration produced by ZT300@15% and T300 under simulated solar light irradiation [15,27]. Figure S8 showed the variation of NBT concentration, and the decrease of NBT concentration indicated the production of  $\text{O}_2^{\cdot-}$ . The production rate of  $\text{O}_2^{\cdot-}$  for ZT300@15% was also much higher than T300 (Fig. 10d). Additionally, the amount of  $\text{H}_2\text{O}_2$  for ZT300@15% was much more than that of T300 (Figure S9), in accord with the result of the  $\text{O}_2^{\cdot-}$  production ( $2\text{O}_2^{\cdot-} + 2\text{H}^+ \rightarrow \text{H}_2\text{O}_2 + \text{O}_2$ ) [25]. By analyzing these results, it could be found that ZT300 nanocomposite was beneficial for the separation of photogenerated electron-hole pairs and production of  $\cdot\text{OH}$  and  $\text{O}_2^{\cdot-}$ , which might be the main reason that ZT300 exhibited excellent photocatalytic activity toward the MO degradation.

To further investigate the roles of these active species such as electrons-holes,  $\cdot\text{OH}$  and  $\text{O}_2^{\cdot-}$  in photocatalytic degradation

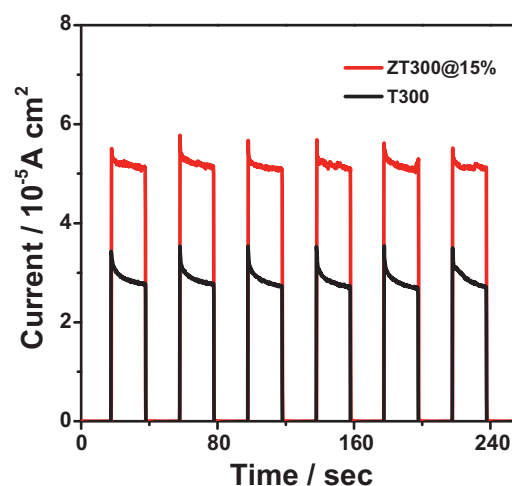


**Fig. 9.** Transient photocurrent responses of T300 and ZT300@15% nanocomposite in 0.1 M  $\text{Na}_2\text{SO}_4$  aqueous solution without bias versus Pt electrode under simulated solar light irradiation.

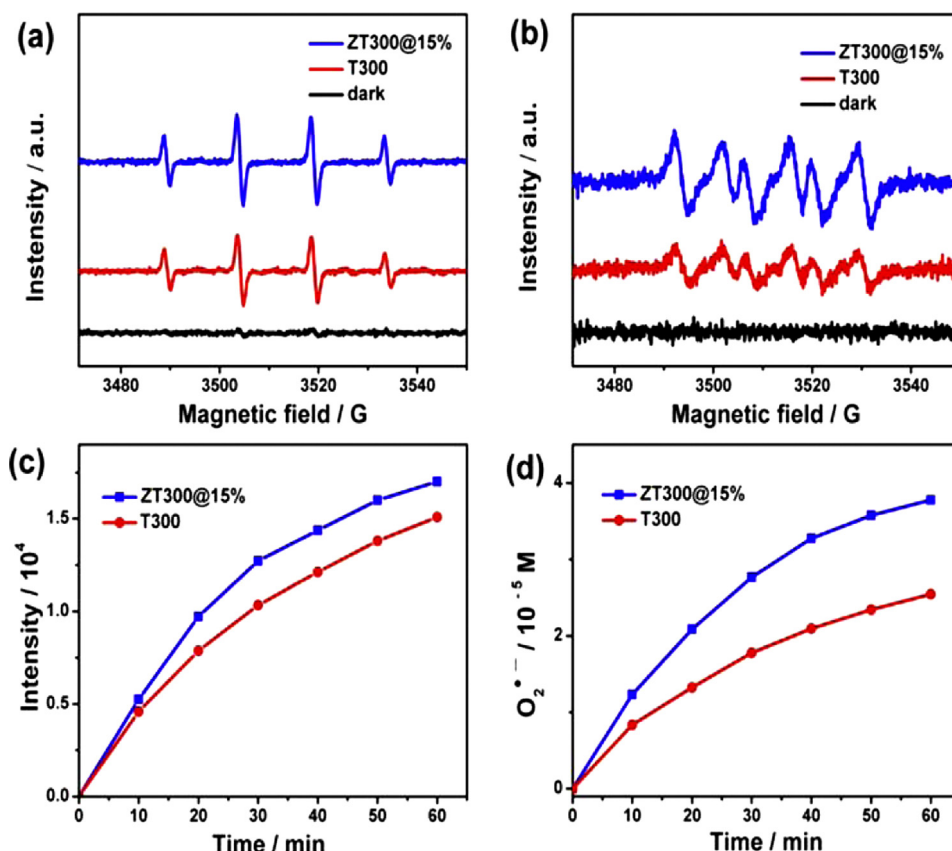


**Fig. 10.** (a) DMPO–OH<sup>•</sup> and (b) DMPO–O<sub>2</sub><sup>•-</sup> measured by DMPO spin-trapping ESR spectra for T300 and ZT300@15%. (c) •OH-trapping PL intensity of ZT300@15% and T300 in TA solution. (d) Change of O<sub>2</sub><sup>•-</sup> concentration for ZT300@15% and T300 under simulated solar light irradiation (320 nm < λ < 800 nm).

process, different types of active species scavengers were added in catalyst system. Fig. 11 showed the photocatalytic activity of ZT300@15% nanocomposite toward the MO degradation under the different conditions. The benzoquinone (BQ) has the ability to trap O<sub>2</sub><sup>•-</sup> by a simple electron transfer mechanism [34]. The addition of BQ (0.1 mg) provoked the most inhibition of the MO degradation, illuminating that O<sub>2</sub><sup>•-</sup> played the most important role in the degradation process. After 0.015 g of ammonium oxalate (AO) as a hole-scavenger being added into the reaction system [35], the decrease in the rate of degradation of MO over ZT300@15% was serious, which meant the photogenerated holes might play an

important role in the photocatalytic degradation. After 250 μL of *tert*-butyl alcohol (TBA) as a scavenger for •OH being added in the system [36], it partially impacted the decomposition rate. So, the MO degradation was driven by the contribution of •OH radicals to a lesser extent. Based on the integrated analysis of these results, it can be concluded that the MO degradation was driven mainly by the participation of O<sub>2</sub><sup>•-</sup> radicals and holes, •OH radicals to a lesser extent.

Based on the results of photoelectrochemical measurement, ESR spin-trapping technique, DPD method and the addition of active species scavengers, the mechanism for photocatalytic degradation of MO on ZT300 nanocomposite was proposed and represented in Scheme 1. For ZT300 nanocomposite, ZnO NPs were uniformly grafted on the surface of TiO<sub>2</sub>-PC to form the heterojunction due

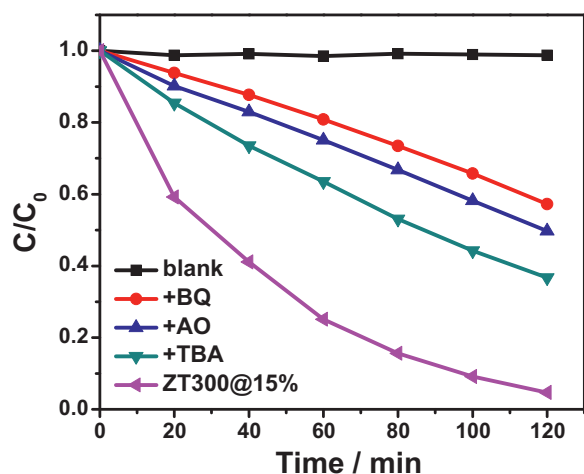
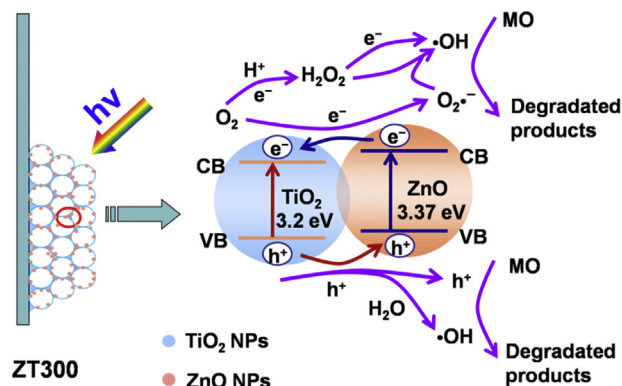


**Fig. 11.** Effect of different scavengers on the photocatalytic degradation of MO over ZT300@15% nanocomposite under simulated solar light illumination.



**Scheme 1.** Schematic diagram illustrating the charge-transfer process in the ZT300 nanocomposite under simulated solar light irradiation.



to intimate interfacial contact between TiO<sub>2</sub> and ZnO NPs. Under simulated solar light irradiation, the photogenerated electrons transferred from the conduction band (CB) of ZnO to the conduction band of TiO<sub>2</sub> under illumination, meanwhile the photogenerated holes transferred from the valence band (VB) of TiO<sub>2</sub> to the valence band of ZnO [37–40]. It effectively separated the electrons and holes, and accordingly increased the lifetime of the charge carriers, in which electrons reduced the dissolved molecular oxygen to produce O<sub>2</sub><sup>•−</sup> (O<sub>2</sub> + e → O<sub>2</sub><sup>•−</sup>), while holes oxidized H<sub>2</sub>O molecular to yield •OH (h<sup>+</sup> + H<sub>2</sub>O → •OH + H<sup>+</sup>). Because of the separation of the photogenerated electrons and holes, more O<sub>2</sub><sup>•−</sup> radicals (O<sub>2</sub> + e → O<sub>2</sub><sup>•−</sup>) and holes were produced, improving the photocatalytic activity. From the Scheme, it can be found that O<sub>2</sub><sup>•−</sup>, holes and •OH played important roles in the MO degradation. Therefore, the photonic crystal structure improved the light harvesting, and heterostructure enhanced the separation efficiency of photogenerated electron–hole pairs. These were the reasons that ZnO/TiO<sub>2</sub> photonic crystal possessed high activity and stability.

#### 4. Conclusions

Three-dimensional highly ordered ZnO/TiO<sub>2</sub>-PC nanocomposite could be fabricated via a facile pyrolysis approach. ZnO NPs were uniformly grafted on the surface of TiO<sub>2</sub>-PC to form the heterojunction due to intimate interfacial contact between TiO<sub>2</sub> and ZnO NPs. Moreover, the ZnO/TiO<sub>2</sub>-PC nanocomposite performed superior photocatalytic activities to its counterparts of ZnO film, TiO<sub>2</sub>-PC film, and P25 particulate film. The enhanced photocatalytic activities could be primarily attributed to the formation of heterojunction structure in the interface between ZnO and TiO<sub>2</sub>-PC, which greatly promoted the efficient separation of photogenerated electron–hole charge carriers. More significantly, the ZnO/TiO<sub>2</sub>-PC hybrid system possessed excellent photostability and could be readily recovered owing to the periodic photonic structures of ZnO/TiO<sub>2</sub>-PC. At last, the roles of active species played in the photocatalytic process were investigated, and the possible degradation mechanism of ZnO/TiO<sub>2</sub>-PC was proposed and discussed.

#### Acknowledgments

This work was financially supported by the National Natural Science Foundation of China (21173047 and 21373049), and National Basic Research Program of China (973 Program, 2013CB632405).

#### Appendix A. Supplementary data

Supplementary data associated with this article can be found, in the online version, at <http://dx.doi.org/10.1016/j.apcatb.2015.01.001>.

#### References

- [1] A. Fujishima, T.N. Rao, D.A. Tryk, J. Photochem. Photobiol. C: Photochem. Rev. 1 (2000) 1–21.
- [2] M.R. Hoffmann, S.T. Martin, W. Choi, D.W. Bahnemann, Chem. Rev. 95 (1995) 69–96.
- [3] J.Z. Chen, W.Y. Ko, Y.C. Yen, P.H. Chen, K.J. Lin, ACS Nano 6 (2012) 6633–6639.
- [4] S.A. Berhe, S. Nag, Z. Molinets, W.J. Youngblood, ACS Appl. Mater. Interfaces 5 (2013) 1181–1185.
- [5] N. Lu, X. Quan, J. Li, S. Chen, H. Yu, G. Chen, J. Phys. Chem. C 111 (2007) 11836–11842.
- [6] T. Sasaki, S. Nakano, S. Yamauchi, M. Watanabe, Chem. Mater. 9 (1997) 602–608.
- [7] X. Chen, S.S. Mao, Chem. Rev. 107 (2007) 2891–2959.
- [8] X. Jiang, T. Herricks, Y. Xia, Adv. Mater. 15 (2003) 1205–1209.
- [9] H. Choi, M.G. Antoniou, M. Pelaez, A.A. de la Cruz, J.A. Shoemaker, D.D. Dionysiou, Environ. Sci. Technol. 41 (2007) 7530–7535.
- [10] J. Liu, G. Liu, M. Li, W. Shen, Z. Liu, J. Wang, J. Zhao, L. Jiang, Y. Song, Energy Environ. Sci. 3 (2010) 1503.
- [11] C. Cheng, S.K. Karuturi, L. Liu, J. Liu, H. Li, L.T. Su, A.I.Y. Tok, H.J. Fan, Small 8 (2012) 37–42.
- [12] E.S. Kwak, W. Lee, N.-G. Park, J. Kim, H. Lee, Adv. Funct. Mater. 19 (2009) 1093–1099.
- [13] H. Li, Q. Tang, F. Cai, X. Hu, H. Lu, Y. Yan, W. Hong, B. Zhao, Sol. Energy 86 (2012) 3430–3437.
- [14] X. Zheng, S. Meng, J. Chen, J. Wang, J. Xian, Y. Shao, X. Fu, D. Li, J. Phys. Chem. C 117 (2013) 21263–21273.
- [15] X. Zheng, D. Li, X. Li, L. Yu, P. Wang, X. Zhang, J. Fang, Y. Shao, Y. Zheng, Phys. Chem. Chem. Phys. 16 (2014) 15299–15306.
- [16] M.A. Fox, M.T. Dulay, Chem. Rev. 93 (1993) 341–357.
- [17] J. Xu, B. Yang, M. Wu, Z. Fu, Y. Lv, Y. Zhao, J. Phys. Chem. C 114 (2010) 15251–15259.
- [18] Y. Lu, H. Yu, S. Chen, X. Quan, H. Zhao, Environ. Sci. Technol. 46 (2012) 1724–1730.
- [19] J. Liu, M. Li, J. Wang, Y. Song, L. Jiang, T. Murakami, A. Fujishima, Environ. Sci. Technol. 43 (2009) 9425–9431.
- [20] N. Wang, C. Sun, Y. Zhao, S. Zhou, P. Chen, L. Jiang, J. Mater. Chem. 18 (2008) 3909.
- [21] B.S. Shaheen, H.G. Salem, M.A. El-Sayed, N.K. Allam, J. Phys. Chem. C 117 (2013) 18502–18509.
- [22] A.A. Khodja, T. Sehili, J.-F. Pilichowski, P. Boule, J. Photochem. Photobiol. A: Chem. 141 (2001) 231–239.
- [23] Y. Lei, G. Zhao, M. Liu, Z. Zhang, X. Tong, T. Cao, J. Phys. Chem. C 113 (2009) 19067–19076.
- [24] F.X. Xiao, ACS Appl. Mater. Interfaces 4 (2012) 7055–7063.
- [25] T. Hirakawa, Y. Nosaka, Langmuir: ACS J. Surf. Colloids 18 (2002) 3247–3254.
- [26] W. Li, D. Li, Y. Lin, P. Wang, W. Chen, X. Fu, Y. Shao, J. Phys. Chem. C 116 (2012) 3552–3560.
- [27] E. Gao, W. Wang, Nanoscale 5 (2013) 11248–11256.
- [28] H.S. Choi, J.W. Kim, Y.N. Cha, C. Kim, J. Immunoassay Immunochem. 27 (2006) 31–44.
- [29] H. Bader, V. Sturzenegger, J. Hoigné, Water Res. 22 (1988) 1109–1115.
- [30] F. Xiao, J. Mater. Chem. 22 (2012) 7819.
- [31] A. Ye, W. Fan, Q. Zhang, W. Deng, Y. Wang, Catal. Sci. Technol. 2 (2012) 969.
- [32] S. Yang, X. Quan, X. Li, Y. Liu, S. Chen, G. Chen, Phys. Chem. Chem. Phys. 6 (2004) 659.
- [33] C. Chen, P. Lei, H. Ji, W. Ma, J. Zhao, H. Hidaka, N. Serpone, Environ. Sci. Technol. 38 (2004) 329–337.
- [34] R. Palominos, J. Freer, M.A. Mondaca, H.D. Mansilla, J. Photochem. Photobiol. A: Chem. 193 (2008) 139–145.
- [35] W. Li, D. Li, W. Zhang, Y. Hu, Y. He, X. Fu, J. Phys. Chem. C 114 (2010) 2154–2159.
- [36] J. Wang, P. Wang, Y. Cao, J. Chen, W. Li, Y. Shao, Y. Zheng, D. Li, Appl. Catal. B: Environ. 136–137 (2013) 94–102.
- [37] B. Liu, Y. Sun, D. Wang, L. Wang, L. Zhang, X. Zhang, Y. Lin, T. Xie, RSC Adv. 4 (2014) 32773.
- [38] L. Lin, Y. Yang, L. Men, X. Wang, D. He, Y. Chai, B. Zhao, S. Ghoshroy, Q. Tang, Nanoscale 5 (2013) 588–593.
- [39] L. Yang, Y. Q.-I. Ma, Cai, Y.M. Huang, Appl. Surf. Sci. 292 (2014) 297–300.
- [40] T.J. Athauda, J.G. Neff, L. Sutherland, U. Butt, R.R. Ozer, ACS Appl. Mater. Interfaces 4 (2012) 6917–6926.